Synthesis of $BiVO_4$ and $Au/BiVO_4$ nanocomposites to achieve the visible-light-driven photocatalytic reduction of Cr^{+6} in pure and tap water – Optimization of the reaction conditions

Juan C. Durán-Álvarez (carlos.duran@icat.unam.mx)
Universidad Nacional Autonoma de Mexico https://orcid.org/0000-0002-5247-6719
Drisya Karathuparathottathil
Universidad Nacional Autonoma de Mexico
Rodrigo García-Tablas
Universidad Nacional Autonoma de Mexico
Luis Lartundo-Rojas
Instituto Politecnico Nacional Unidad Zacatenco
Myriam Solís-López
CINVESTAV: Centro de Investigacion y de Estudios Avanzados del Instituto Politecnico Nacional
Rodolfo Zanella
Universidad Nacional Autonoma de Mexico
Velumani Subramaniam
CINVESTAV: Centro de Investigacion y de Estudios Avanzados del Instituto Politecnico Nacional

Research Article

Keywords: heavy metals, hydrothermal method, photocatalysis, sacrificial agent, water purification

Posted Date: May 27th, 2022

DOI: https://doi.org/10.21203/rs.3.rs-1595043/v1

Abstract

Heterogeneous photocatalysis is used to mineralize organic pollutants and inactivate pathogens in water, whereas the removal of heavy metals is less explored. In this work, $BiVO_4$ was synthesized through the hydrothermal route to achieve the photocatalytic reduction of Cr^{+6} in water. Monoclinic $BiVO_4$ displayed high crystallinity and a fern-leaf-like form; specific surface area and bandgap energy were determined as 5.68 m^2 g^{-1} and 2.49 eV, respectively. Surface plasmon resonance was identified in the Au/$BiVO_4$ nanocomposites, while the specific surface was reduced to 3.16 m^2 g^{-1} after the deposition of gold nanoparticles. Different sacrificial agents were tested to boost the photocatalytic performance of $BiVO_4$, including methanol, ethanol, formic acid, dimethyl sulfoxide, and KI, finding the best results with 0.01 M formic acid. The optimal photocatalyst dosage was 1.5 g L^{-1}, achieving the complete photoreduction of Cr^{+6} after 90 min of visible light irradiation. No improvement in the photocatalytic activity was observed when metallic gold nanoparticles were deposited on $BiVO_4$ nanocomposites, more likely due to the reduced specific surface area. Chromium was precipitated on the $BiVO_4$ surface as Cr^{+3}, Cr^{+4} and Cr^{+5} oxidized species. The catalyst displayed high stability across three consecutive reaction cycles, and good performance was observed in tap water, with the complete photoreduction of Cr^{+6} upon 2 h of visible light irradiation. Purging dissolved O_2 from the water was an essential factor to achieve the highest photocatalytic performance.

Introduction

Chromium is the 21st most abundant element on the Earth's crust; it occurs in oxidation states from +6 to -2 (Matrosova et al. 2020). In water, the oxidation of Cr^{+3} to Cr^{+6} is not a spontaneous process because of the high oxidation potential of the Cr^{+3}/Cr^{+6} redox pair (-1.33 V vs. NHE), as opposed to the reduction of Cr^{+6} to Cr^{+3} mediated by reducing agents, like Fe^{+2} or dissolved organic matter (Hori et al. 2015); hence, Cr^{+3} prevails in nature over Cr^{+6} (Matrosova et al. 2020). Still, traces of Cr^{+6} have been reported in surface and groundwater reservoirs (Tumolo et al. 2020) via natural and anthropogenic sources (Perraki et al. 2021). This can jeopardize the water and food security in urban and rural settlements due to the deleterious effects this pollutant causes to organisms through the food chain (He and Li 2020). Hexavalent chromium is a group 1 carcinogen, which is able to produce a plethora of harmful effects at the cellular level (DesMarias and Costa 2019). Also, it may cause tissue damage in kidney and liver as well as in the gastric and hematopoietic systems (Teklay 2016). Moreover, using polluted water for agricultural irrigation is prohibited, as Cr^{+6} can be either assimilated by crops posing a risk to consumers (Ugulu et al. 2021) or leachate to groundwater (Tumolo et al. 2020). The US Environmental Protection Agency defined a maximum permissible limit for Cr^{+6} in drinking water at 0.01 mg L^{-1} to avoid acute and chronic toxicity effects in humans; therefore, removing hexavalent chromium from drinking water is a priority. The elimination of Cr^{+6} can be achieved through electrochemical and multibarrier systems (Owlad et al. 2009). Still, these processes are energy-consuming and complex for impoverished regions. Heterogeneous photocatalysis has demonstrated the potential to remove heavy metals from

water, with TiO_2 as the most used semiconductor to reduce hexavalent chromium (Litter 2017). However, this semiconductor is photoactive under UV-A light irradiation, which is less than 5 % of the natural light reaching the troposphere, limiting its use in sunlight driven systems. In addition, the synthetic routes commonly followed to obtain photoactive TiO_2 may produce hazardous residues. Therefore, bismuth-based semiconductors of low bandgap could be an efficient alternative (Meng and Zhang 2016).

Among the bismuth-based semiconductors, bismuth vanadate has gained attention due to its high dispersibility, innocuity, photo-stability, and low bandgap value (around 2.5 eV), resulting in a growing number of reports on its photocatalytic activity in the last two decades (Malathi et al. 2018). $BiVO_4$ has three polymorphs: monoclinic scheelite, tetragonal zircon and tetragonal, among which the monoclinic phase is highly active within the visible range (Saison et al. 2015). The valence band maximum and the conduction band minimum of $BiVO_4$ are comprised of the O 2p and V 3d orbitals, respectively. The reduction potential of the conduction band (-0.26 V vs NHE at pH = 7.0) makes $BiVO_4$ a photocatalyst suitable to perform reduction processes, such as water splitting (Jian et al. 2019) and the conversion of Cr^{+6} into its reduced species (Sun et al. 2014) under visible light irradiation. Moreover, the photocatalytic potential of $BiVO_4$ can be improved by coupling it with metals and semiconductors. For example, Zhao et al. (Zhao et al. 2016) reported up to 76.5 % of Cr^{+6} photoreduction after 90 min of visible light irradiation using the $BiVO_4/MoS_2$ nanocomposite, compared to the lower conversion (12%) achieved when bare $BiVO_4$ was used. Cao et al. (Cao et al. 2012) observed the rise in the photocatalytic performance of $BiVO_4$ microtubes and nanosheets by the deposition of well-dispersed Au nanoparticles. The improvement in the catalytic performance has been attributed to the electron trap effect and the plasmonic resonance effect, which increase the lifetime of the charge carriers by reducing the recombination rate at the time the redox potential of the hole/electron pair is modified (Primo et al. 2011; Van et al. 2015).

So far, the photocatalytic activity of $BiVO_4$ and the $Au/BiVO_4$ has been tested for the degradation of organic pollutants in water (Malathi et al. 2018), whereas the reduction of heavy metals is relatively unexplored. This work aimed to synthesize $BiVO_4$ and $Au/BiVO_4$ to achieve the photocatalytic reduction of Cr^{+6} in pure and tap water under visible light irradiation. Univariate analysis was carried out to optimize the reaction conditions to achieve the highest conversion rate.

Materials And Methods

Synthesis of $BiVO_4$ and $Au/BiVO_4$

Nanosized $BiVO_4$ was synthesized through the hydrothermal method, using a modification of the procedure reported elsewhere (Shen et al. 2010). In brief, 0.1 mol L^{-1} $Bi(NO_3)_3 \cdot 5H_2O$ was prepared in 50 mL of 2 mol L^{-1} HNO_3, then 50 mL of aqueous 0.1 mol L^{-1} NH_4VO_3 were dripped under magnetic stirring. The yellow suspension was heated at 80°C under stirring for another 30 min and transferred into a 150 mL autoclave. Thermal treatment was provided at 200°C for 6 h and then cooled at room temperature.

The precipitate was recovered by ultracentrifugation at 10,500 rpm for 5 min; the supernatant was discarded. The solid was washed four times with 100 mL of distilled water, then dried at 80°C in vacuum (0.08 MPa) for 2.5 h.

The surface of the $BiVO_4$ was modified by the deposition of metallic Au nanoparticles, which were synthesized via the deposition-precipitation method, using urea as basifying agent (Zanella et al. 2002). A 4.2×10^{-3} mol L^{-1} $HAuCl_4\bullet3H_2O$ solution was prepared in distilled water, then 1 g of $BiVO_4$ was added and magnetically stirred at 80°C for 5 min to assure the complete dispersion of the powder. Urea was then added, using a 1:100 Au:urea molar ratio. The reaction lasted 16 h, and at the end, the powder was recovered by ultracentrifugation (10,500 rpm for 5 min); the pH of the supernatant was measured prior to being discarded. The precipitate was washed with 100 mL of distilled water through several cycles until the pH of the supernatant was below 7.0. After the washing cycles, the material was dried at 80°C in vacuum (0.08 MPa) for 2.5 h. Activation of the Au nanoparticles was accomplished by calcination at 500°C, at a ramp of 2°C min^{-1}, under H_2 reducing conditions. The activated material was stored in amber glass vials less than one month prior to use. Three theoretical loadings of Au were deposited on the $BiVO_4$ material, namely 0.5, 1.0, and 1.5 wt. %.

Characterization Of The Materials

The crystallographic analysis was carried out using a Bruker AXS-D8 diffractometer, with a Cu-Kα source (1.54 Å), within a 2θ range from 10 to 70 degrees and a step size of 0.02 degrees. The specific surface area was determined by the Braunauer-Emmet-Teller (BET) approach, using an Autosorb-1 Quantachrome instrument. For this, a 250 mg sample was degassed overnight; then, the N_2 adsorption-desorption analysis was performed under vacuum at -196°C. The morphological analysis was performed by Scanning Electron Microscopy in a SEM-JEOL-JSM 56000 LV instrument. The imaging was carried out at 20 kV with different magnifications. The actual loading of Au nanoparticles deposited on the $BiVO_4$ materials was determined by ICP-OES analysis. The X-ray photoelectron spectroscopic analysis was carried out to identify the chemical species occurring on the surface of the material before and after photocatalysis tests. A Thermo Fisher K-alpha X-ray photoelectronic spectrometer was used for the measurements, at a base pressure of 1×10^{-9} Torr; a monochromatic light source Kα (1486.6 eV) was utilized. X-rays were micro-focused at the source to obtain a spot diameter size of approximately 400 µm in the sample. High-resolution spectra were deconvolved using the Gaussian-Lorentzian function and a Shirley-type baseline. The bandgap energy (E_g) was determined through UV-visible spectroscopy analysis, measuring the diffuse reflectance in an Agilent Cary 5000 UV-vis-NIR spectrophotometer. The spectra were obtained within the wavelength range of 200 to 800 nm, employing the Praying Mantis accessory. The Kubelka-Munk approach was used through Eq. 1.

$$\alpha hv = A(hv - E_g)^{\frac{1}{n}} \quad \text{Eq. 1}$$

Where α is the absorption coefficient, h is Planck's constant, v is the frequency, and A is the light absorption at a given wavelength. The 1/n term varies as a function of the semiconductor inter-band transitions, being ½ for indirect transitions and 1 for direct transitions. In the case of $BiVO_4$, this value was ½.

Photocatalysis Experimental Setup

The photocatalysis tests were carried out in a double walled-glass batch type reactor equipped with temperature control by continuous water circulation. A 20 mg L^{-1} $Cr_2O_7^{-2}$ solution was prepared in distilled water from a 1000 mg L^{-1} stock solution in 2% (v/v) HNO_3. 250 mL of the $Cr_2O_7^{-2}$ solution were filled in the photoreactor. The photocatalyst was added to the solution, and magnetic stirring was provided at 25°C for 30 min in the dark to achieve the adsorption-desorption equilibrium. Air was purged by bubbling 100 mL min^{-1} of high purity N_2. The light source was a 25 W Xenon lamp, with an emission range between 380 and 700 nm, placed 5 cm above the reactor. Irradiation experiments were carried out for 5 h, and 8 mL aliquots were withdrawn after 5, 10, 15, 30, 45, 60, 90, 120, 180, 240, and 300 min of irradiation, as well as at the beginning of the assay. All the liquid samples were filtered using nylon membrane (pore size of 0.45 µm) to separate the catalyst, then acidified using 250 µL of H_3PO_4 and 100 µL of HNO_3 prior to analysis.

The optimization of the reaction conditions was performed through the univariate analysis. The optimal concentration of the catalyst was determined by testing dosages of 0.25, 0.5, 1.0, 1.5, and 2 g L^{-1}. In addition, the sacrificial agent was selected from testing ethanol methanol, potassium iodide, acetic acid, and dimethyl sulfoxide. The optimal concentration of the best sacrificial agent was picked after testing three levels, namely 0.01, 0.04, and 0.1 mol L^{-1}. Lastly, the most efficient loading of Au supported on $BiVO_4$ was determined.

Using the optimal reaction conditions, the photocatalytic reduction of Cr^{+6} was determined in tap water.

Quantification Of Hexavalent Chromium In Water Samples

This determination was performed by UV-visible spectrometry analysis (Lace et al. 2019). The acidified samples were mixed with 2 mL of 1,5-diphenylcarbazide in acetone (0.02 mol L^{-1}). The resulting solution was colored magenta, with the absorbance peak at 543 nm. The absorbance was measured in a Cary 5000 UV-visible-NIR spectrophotometer to further calculate the residual concentration of Cr^{+6} through Eq. 2.

$$C = \frac{A}{\epsilon l}$$ Eq. 2

Where C is the concentration of Cr^{+6} in the sample, A is the absorbance at 543 nm, and ε is the molar absorptivity coefficient. The calibration curve was obtained for a concentration range from 0.1 to 25 mg L^{-1}, as is shown in the Supplementary Information section.

The photocatalytic efficiency was quantitatively determined by calculating the initial reaction rate constant (*k*), fitting the reaction kinetics to the first-order reaction model (Eq. 3)

$$\ln C\mathrm{t} = \ln C\mathrm{o} - kt \quad \text{Eq. 3}$$

Where C_o is the initial concentration of Cr^{+6} (mg L^{-1}), C_t is the Cr^{+6} concentration at time *t* (mg L^{-1}), *k* is the first-order reaction rate constant (min^{-1}), and t is the reaction time. For all the calculations, *k* was determined for the first 60 min of reaction.

Results And Discussion

Characterization of the materials

The structural properties of $BiVO_4$ and Au/$BiVO_4$ materials were measured by X-ray diffraction analysis. The diffraction pattern fitted well with the crystalline monoclinic $BiVO_4$ (JCPDS No. 01-075-1866), displaying lattice parameters of a = 5.193, b = 5.089 and c = 11.69. In the diffraction pattern, the split peak at 18.5° was assigned to the (110) and (011) planes, while signals at 2θ values of 28.9°, 30.54°, 42.49°, and 50.33° corresponded to the (112), (004), (015) and (220) planes (Fig. 1a) (Daniel Abraham et al. 2016; Kamble and Ling 2020). No impurities of other phases, like Bi_2O_3, were observed, while the occurrence of sharp peaks reveled the high crystallinity of the material. The crystallite size was determined by the Scherrer formula as 33.08 nm, which is consistent with reported for other materials synthesized through the hydrothermal route (Obregón et al. 2012; Nguyen and Hong 2020). Regarding the surface-modified material, no peaks corresponding to Au° crystals were detected attributed to the low loading of the nanoparticles (1.5 wt. %), along with their high dispersion on the surface of the $BiVO_4$ nanocrystals (Wei et al. 2019). Other characterizations were carried out to demonstrate the presence of metallic gold nanoparticles on the $BiVO_4$.

According to the microscopic analysis, the $BiVO_4$ nanocrystals presented structures resembling fern leaves (Fig. 1b-c), while no changes in the morphology were observed upon the decoration with Au° nanoparticles (Figs. 1d). The metallic gold nanoparticles were faintly observed when the loading was higher than 1 wt. %, showing high dispersion on the surface of the $BiVO_4$ leaves. Elemental analysis by EDX and ICP-OES demonstrated that deposition of Au° nanoparticles occurred with an efficiency above 90% (Table S1). Similar results have been reported for the deposition of Au° nanoparticles on other semiconductors, like TiO_2 and BiOI, using the same synthetic method (Oros-Ruiz et al. 2014; Durán-Álvarez et al. 2016, 2020).

The specific surface area of unmodified $BiVO_4$ was determined as 5.68 $m^2\ g^{-1}$, while this value decreased to 3.16 $m^2\ g^{-1}$ when the (1 wt. %) $Au/BiVO_4$ sample was analyzed. This result suggests that Au° nanoparticles occupy the active sites on the $BiVO_4$ surface. Indeed, the specific surface area of the materials obtained in this work seems low, although such values are higher than those reported for $BiVO_4$ aggregates synthesized through other routes, like precipitation (Xu et al. 2009), ultrasonic spray pyrolysis, and even commercially available materials (Alfa-Aesar) (Dunkle et al. 2009). The increased specific surface area of the herein synthesized $BiVO_4$ was achieved using the hydrothermal process with moderate heating time, which has previously been demonstrated to produce nanocrystals with high surface area (Obregón et al. 2012). A type-IV adsorption-desorption isotherm was observed in the BET characterization (See Supplementary Information), with a desorption hysteresis loop typical of mesoporous materials. The average pore diameter was also impacted by the deposition of Au° nanoparticles, decreasing from 6.32 to 5.08 nm for $BiVO_4$ and (1 wt. %) $AuBiVO_4$, respectively. Certainly, reducing the specific surface area of the semiconductor can negatively impact the photocatalysis process, however, a significant decrease in the performance of the surface-modified photocatalysts has not been observed in previous studies (Zanella et al. 2017), implying that the benefits of forming Au/semiconductor nanocomposites surpass the impacts caused by the decrease of the specific surface area.

The light absorption edge of the synthesized $BiVO_4$ was found at 512 nm, resulting in an E_g value of 2.49 eV (Fig. 1e-f). This result indicated that the material can be activated under visible light irradiation, consistent with a previous report (Kamble and Ling 2020). A blue shift in the absorption edge was observed for the $Au/BiVO_4$ sample, probably due to the light screening caused by the Au° nanoparticles distributed over the surface of the $BiVO_4$ nanocrystals. Even though gold nanoparticles decreased the light absorption of $BiVO_4$, the semiconductor can still be photoactivated under visible light irradiation. Moreover, a band centered at 627 nm, corresponding to the surface plasmon resonance, was detected in the absorption spectrum of the (1 wt. %) $Au/BiVO_4$ sample (Fig. 1e), corroborating the occurrence of tiny (2 to 50 nm) and well dispersed Au° nanoparticles on the surface of the semiconductor (Amendola et al. 2017). This trait could increase the photocatalytic performance of the nanocomposite compared to the unmodified material (Primo et al. 2011; Wei et al. 2019).

Chemical analysis by XPS showed the occurrence of Au, Bi, O, and V elements in the samples, as in the low-resolution spectrum (Supplementary Information). The high-resolution spectrum of Bi $4f_{5/2}$ and $4f_{7/2}$ displayed the characteristic double peak at binding energies of 158.7 and 164.2 eV, respectively (Fig. 1g). The separation of the Bi 4f signals by approximately 6.0 eV indicated the trivalent oxidation state of bismuth (Kamble and Ling 2020). In the case of the O 1s, an asymmetrical peak centered at 530.2 eV was obtained (Fig. 1h). The contribution at 532.9 eV was assigned to the occurrence of superficial OH groups from adsorbed water molecules (Jaihindh et al. 2019). The peak at 530.7 eV is usually ascribed to the occurrence of oxygen vacancies on the surface of $BiVO_4$, which are able to improve the photocatalytic

activity of the material by increasing the lifetime of the photogenerated charge carriers (Kalanur and Seo 2022).

Regarding the gold high-resolution XP spectrum, the peaks at 84 and 87.7 eV were assigned to Au $4f_{5/2}$ and Au $4f_{7/2}$, respectively (Wei et al. 2019). The doublet separation presented an energy difference of 3.7 eV, indicating that Au was in its metallic state (Jayaraj and Paramasivam 2019). Small contributions at 83.3 and 86.8 eV were found after deconvolution, which was ascribed to the Au-V bonds (Fig. 1i). In contrast, peaks at 84.8 and 88.6 eV indicated the occurrence of some chloride residues from the synthesis step (Yu et al. 2017).

Photocatalytic Tests

The photolytic reduction of hexavalent chromium through 5 h of visible light irradiation was determined to establish a baseline to compare the performance of the synthesized photocatalysts. No significant decrease in the Cr^{+6} concentration was noted through the photolysis test, contrary to that observed when 0.5 g L^{-1} of $BiVO_4$ was used. For the latter, the complete removal of Cr^{+6} was achieved after 180 min of visible light irradiation. Previous studies have reported negligible removal of Cr^{+6} under visible (Jaihindh et al. 2019) and UV light irradiation (Zhang et al. 2020), therefore developing photocatalysts to efficiently treat heavy metals is a matter of research. Moreover, the proposed photocatalysts should work under optimal conditions (e.g., the type and concentration of the sacrificial agent, the photocatalyst dosage, and so forth) so the highest performance can be reached. Therefore, optimization should be the natural step prior to testing the photocatalysts under realistic or upscaled conditions.

Optimization Of The Sacrificial Agent

Different sacrificial agents were tested to aid in the photocatalytic reduction of Cr^{+6} by scavenging both photoholes and reactive oxygen species produced by $BiVO_4$, which can re-oxidize Cr^{+3} to Cr^{+6} (Liang et al. 2021). In these experiments, 0.5 g L^{-1} of $BiVO_4$ was used, and the reaction medium was composed of 80% of the $Cr_2O_7^{-2}$ solution and 20% of the sacrificial agent. For KI and formic acid, the reaction media was made up of 0.4 mol L^{-1} aqueous solution of the sacrificial agent. As shown in Fig. 2, using formic acid resulted in the highest photocatalytic activity ($k = 7.2\times10^{-3}$ min^{-1}), with the complete reduction of Cr^{+6} in 180 min. Lower photocatalytic conversion was obtained when potassium iodide ($k = 4.1\times10^{-3}$ min^{-1}), an inorganic salt commonly used as a photohole scavenger, was tested. Reaction rate constants (k) of 9×10^{-4}, $5.1\times10^{-3,}$ and 4.7×10^{-4} min^{-1} were calculated when methanol, DMSO, and ethanol were used as sacrificial agents, respectively (Table S2). Formic acid has been systematically reported as a suitable sacrificial agent able to scavenge photoholes (Chen et al. 2012; Dozzi et al. 2012; Islam et al. 2019, 2021), undergoing mineralization to CO_2, with no formation of stable byproducts that can further react with the reduced chromium species or with the catalyst. Indeed, non-aromatic carboxylic acids

increase the reaction rate constant since carboxylic moieties directly insert electrons into the semiconductor valence band, neutralizing the photoholes (Colón et al. 2001). Due to its low oxidation potential and higher relative permittivity, formic acid turned out as a better sacrificial agent than alcohols and dimethyl sulfoxide (Wang et al. 2017).

The concentration of formic acid was varied to maximize the photocatalytic Cr^{+6} reduction. Increasing the concentration from 0.04 to 0.1 mol L^{-1} resulted in a slight increase in the reaction rate constant, from $k = 2.57\times10^{-2}$ min^{-1} to $k = 3.3\times10^{-2}$ min^{-1}. However, the highest k value was found when the formic acid concentration decreased to 0.01 mol L^{-1}, resulting in 4.93×10^{-2} min^{-1} (Table S2). Further decrease in the concentration of the sacrificial agent resulted in a drop in the reaction rate constant, hence the optimal concentration of formic acid was set as 0.01 mol L^{-1}, which is in line with the previous reports (Rengaraj et al. 2007; Chen et al. 2012).

The photocatalytic reduction of Cr^{+6} occurs as indicated in Eq. 4

$$Cr_2O_7^{-2} + 14H^+ + 6e^- \longrightarrow 2Cr^{+3} + 7H_2O \qquad \text{Equation 4}$$

In this reaction, 6 mol of photoelectrons are consumed by each mol of $Cr_2O_7^{-2}$. Since formic acid reacts with photoholes, blocking the recombination and impeding the reoxidation of Cr^{+6}, therefore six mol of the sacrificial agent are necessary to achieve maximum efficiency. In the reaction system used in this work, 0.01 mmol of $Cr_2O_7^{-2}$ requires 0.06 mmol of photoelectrons to be completely reduced, and thus 2.5 mmol of formic acid (i.e., 0.01 mol L^{-1} in 250 mL) are enough to completely consume photoholes, fostering the reaction of photoelectrons with the Cr^{+6} adsorbed on the photocatalyst surface. It is possible that when the concentration of formic acid was increased up to 0.04 and 0.1 mol L^{-1} competence by adsorption sites occurred leading to a diminished reaction rate constant.

Optimization Of The Catalyst Loading

Different loadings of $BiVO_4$ were tested, finding the highest performance with 1.5 g L^{-1} (Fig. 3). This result is similar to that reported in previous studies using $BiVO_4$ for the photocatalytic removal of organic pollutants (Xu et al. 2009; Shen et al. 2010; Obregón et al. 2012). The complete reduction of Cr^{+6} was achieved after 90 min of visible light irradiation using the optimal dosage, and it took 4 h with the lowest dose (0.25 g L^{-1}). It can be explained by low specific surface area of the material, and thus a higher dose of the photocatalyst is necessary to efficiently adsorb most of the Cr^{+6} in the solution. On the contrary, when a $BiVO_4$ dosage of 2 g L^{-1} was tested, the screening effect occurred, increasing the time for the complete reduction of Cr^{+6} up to 2 h. The initial reaction rate constant was calculated for the tested

conditions (Table 1), displaying the following order 1.5 g L^{-1} > 2 g L^{-1} > 1 g L^{-1} > 0.5 g L^{-1} > 0.25 g L^{-1}. Negligible reduction of Cr^{+6} was obtained in photolysis tests, as was pointed out above.

Table 1
Photocatalytic reaction rate using different dosage of $BiVO_4$ and different Au loadings

Material	Dosage (g L^{-1})	k (min^{-1})
$BiVO_4$	0.25	6.8×10^{-3}
	0.5	1.18×10^{-2}
	1.0	1.97×10^{-2}
	1.5	4.99×10^{-2}
	2.0	3.5×10^{-2}
(0.5 wt. %) Au/$BiVO_4$	1.5	4.13×10^{-2}
(1.0 wt. %) Au/$BiVO_4$		4.4×10^{-2}
(1.5 wt. %) Au/$BiVO_4$		2.67×10^{-2}

During the adsorption step, before irradiation, the amount of Cr^{+6} retained on the $BiVO_4$ particles was determined as 1%, when the dose of the photocatalyst was 1.5 g L^{-1}. In comparison, 0.34% was accounted for the lowest dosage (0.25 g L^{-1}). This indicates that the low specific surface area of the $BiVO_4$ material highly impacted the photocatalytic performance. Thus, further studies must aim at increasing the surface area of this semiconductor, by the synthesis of 3D structures for instance.

The adsorption of Cr^{+6} is directly related to the superficial charge of the $BiVO_4$ particles, which is pH-dependent. Throughout the photocatalytic process, the pH of the suspension was steady at 2.91. The isoelectric point of the $BiVO_4$ material is 4.26, and at this pH condition, the $BiVO_4$ nanoparticles were positively charged, favoring the adsorption of the $Cr_2O_7^{-2}$ ions through electrostatic interactions. The potential of both the conduction band of $BiVO_4$ and Cr^{+6} is also pH-dependent. For Cr^{+6}, the reduction potential at pH = 3.0, is 0.93 V (vs NHE), while the conduction band level of $BiVO_4$ is 0.32 V (vs NHE) at pH = 0 (Wang et al. 2015). Through the Nernst equation (Eq. 5), the reduction potential of the $BiVO_4$ conduction band at pH = 3 was calculated as 0.143 V (Xie et al. 2006).

$$E\mathrm{CB} = 0 - (0.059 \times pH) \quad \text{Eq. 5}$$

Given that the reduction potential of the conduction band resulted more negative than that of Cr^{+6} the photocatalytic reduction takes place at the pH of the suspension.

Photocatalytic performance of the Au/$BiVO_4$ materials

The photocatalytic reduction of Cr^{+6} was tested using the Au/$BiVO_4$ materials under optimal reaction conditions, assuming that Au° nanoparticles would increase the photocatalytic activity (Primo et al. 2011; Cao et al. 2012). Contrary to the expectations, the surface modified materials displayed a lower conversion compared to unmodified $BiVO_4$ (Table 1). The rate constant displayed by the (1 wt. %) Au/$BiVO_4$ nanocomposite was very similar to that observed when unmodified $BiVO_4$ was used, then a drastic drop in the conversion rate occurred when the (1.5 wt. %) Au/$BiVO_4$ catalyst was tested. This result was surprising, considering the increased photocatalytic activity of Au/$BiVO_4$ nanocomposites reported to degrade organic molecules in water (Zhang and Zhang 2010; Cao et al. 2012). The blockage of the active sites on the $BiVO_4$ surface by Au° nanoparticles is the most plausible explanation. Upon this obstruction, the adsorption of $Cr_2O_7^{-2}$ ions would be reduced in Au/$BiVO_4$ nanocomposites due to the lack of surface charge of the Au° nanoparticles.

Stability Of The Photocatalyst

The photocatalytic activity of the nanosized $BiVO_4$ material was tested in three consecutive reaction cycles. Before cycles 2 and 3, the solid material was recovered from the reaction chamber and the membranes used to filter the samples throughout the reaction. The suspension was centrifuged at 10,500 rpm for 5 min and the supernatant was discarded. No washing was applied to the solid prior to drying at 80°C for 2 h. The photocatalytic performance was steady during the second reaction cycle, while the reaction rate constant dropped by 12% in the third cycle (Fig. 4a and Table S3). The decay in the photocatalytic reduction of Cr^{+6} has been previously reported by Jaihindh et al. (Jaihindh et al. 2019) using shuriken-like $BiVO_4$ nanoparticles. Such behavior can be, on one hand, due to loss of the catalyst during the recovery step. On the other hand, the active sites on the $BiVO_4$ surface could be blocked by adsorbed chromium species, which accumulate over the consecutive reaction cycles.

After the reuse test, the photocatalyst was recovered, dried, and analyzed by XPS to determine the occurrence and speciation of chromium. As shown in Fig. 4b, oxidized chromium species, like oxides, hydroxides, and oxyhydroxides were identified on the $BiVO_4$ surface. The identification of traces of Cr^{+4} and Cr^{+5} indicated the partial photocatalytic reduction of Cr^{+6} to Cr^{+3}. In the high-resolution XP spectrum shown in Fig. 4b, the contributions centered at 584.7 and 575.4 eV could be ascribed to the Cr-N bond [52], indicating the occurrence of residues of nitrate precursors remaining on the $BiVO_4$ surface.

Photocatalytic Activity In Tap Water

Under the optimal reaction conditions, the photocatalytic reduction of Cr^{+6} was carried out in tap water. A slightly lower reaction rate constant was found in tap water vis-á-vis that observed in experiments using

distilled water, 4.64×10^{-2} and 4.88×10^{-2} min^{-1}, respectively. The drop in the conversion rate can be attributed to the matrix composition, including dissolved ions and organic matter (Table S4), which either compete with Cr^{+6} for the adsorption sites on the $BiVO_4$ surface or scavenge the photoelectrons produced upon irradiation. Given the slight difference in the reaction kinetics (Fig. 5), it is possible to assert that matrix had little to no effect on the photocatalytic reduction of Cr^{+6}. In a further experiment, no N_2 bubbling was supplied to purge dissolved O_2 from tap water through the photocatalysis process, resulting in a marked drop of the reaction efficiency ($k = 1.18\times10^{-2}$ min^{-1}). This result shows that dissolved oxygen acts as a strong photoelectron scavenger more than the dissolved components in tap water. When O_2 reacts with photoelectrons in the $BiVO_4$ conduction band, the radical superoxide ($^{\bullet}O_2^{-}$) is formed, which can further react with water molecules to produce hydroxyl radicals ($^{\bullet}OH$) (Xu et al. 2018). These reactive oxygen species can re-oxidize Cr^{+3} (Liang et al. 2021). Overall, dissolved oxygen inhibits the photocatalytic reduction of Cr^{+6} by scavenging photoelectrons and re-oxidizing the reduced chromium species.

Conclusion

Monoclinic $BiVO_4$ was synthesized through the hydrothermal method obtaining fern-leaf-like structures photoactive under visible light irradiation. The photocatalytic activity of the material was assessed through the reduction of hexavalent chromium, finding the complete conversion under visible light irradiation. The optimization of the reaction conditions showed that 0.01 mol L^{-1} formic acid is the best sacrificial agent, along with a photocatalyst dosage of 1.5 g L^{-1}, resulted in the complete reduction of Cr^{+6} after 90 min of irradiation. Depositing Au° nanoparticles on the $BiVO_4$ surface hasn't favored the photocatalytic reduction of Cr^{+6}, more likely because metallic nanoparticles reduce the adsorption of $Cr_2O_7^{-2}$ ions on the photocatalyst surface. Due to this, either the electron trapping effect or the surface plasmon resonance exerted by the metallic nanoparticles are unable to boost the photocatalytic performance of the semiconductor. The photocatalytic reduction of Cr^{+6} to Cr^{+3} was rather partial since some Cr^{+4} and Cr^{+5} species were identified on the photocatalyst surface after three consecutive reaction cycles. Even though chromium was precipitated on the $BiVO_4$ surface, the catalytic activity of the material remained nearly stable, even after the re-use cycles, indicating that specific surface area is an important, but not crucial, factor in the photocatalytic performance of the synthesized $BiVO_4$ material.

Declarations

Acknowledgement: The authors would like to acknowledge the valuable contributions of the M. Sc. Javier Tadeo from Laboratorio de Espectroscopia Atómica and M. Sc. Viridiana Maturano from the Laboratorio Universitario de Nanotecnología Ambiental.

Funding: This work was supported by the Secretaría de Educación, Ciencia, Tecnología e Innovación de la Ciudad de México (SECTeI) and the Consejo Nacional de Ciencia y Tecnología (CONACyT) (grant

numbers SECITI/047/2016 and 263043, respectively).

Authors contribution: All authors contributed to the study conception and design. Material preparation, data collection and analysis were performed by R. García-Tablas, L. Lartudno-Rojas, M. Solís-López and K.T. Drisya. The first draft of the manuscript was written by J.C. Durán-Álvarez, while R. Zanella and S. Velumani reviewed it. All authors commented on previous versions of the manuscript. All authors read and approved the final manuscript.

Data availability: All the data used for the redaction is included within the manuscript

Ethics approval and consent to participate: Not applicable

Consent for publication: All the authors have consented the content of the manuscript for publication

Conflict of interest: The authors have no financial and non- financial interests to declare

References

1. Amendola V, Pilot R, Frasconi M et al (2017) Surface plasmon resonance in gold nanoparticles: a review. J Phys Condens Matter. https://doi.org/https://doi.org/10.1088/1361-648X/aa60f3. 29:
2. Cao SW, Yin Z, Barber J et al (2012) Preparation of Au-$BiVO_4$ heterogeneous nanostructures as highly efficient visible-light photocatalysts. ACS Appl Mater Interfaces 4:418–423. https://doi.org/10.1021/am201481b
3. Chen G, Sun M, Wei Q et al (2012) Efficient photocatalytic reduction of aqueous Cr(VI) over $CaSb_2O_5(OH)_2$ nanocrystals under UV light illumination. Appl Catal B Environ 125:282–287. https://doi.org/10.1016/j.apcatb.2012.06.001
4. Colón G, Hidalgo MC, Navío JA (2001) Influence of carboxylic acid on the photocatalytic reduction of Cr(VI) using commercial TiO_2. Langmuir 17:7174–7177. https://doi.org/10.1021/la010778d
5. Cooper JK, Gul S, Toma FM et al (2015) Indirect bandgap and optical properties of monoclinic bismuth vanadate. J Phys Chem C 119:2969–2974. https://doi.org/10.1021/jp512169w
6. Daniel Abraham S, Theodore David S, Biju Bennie R et al (2016) Eco-friendly and green synthesis of $BiVO_4$ nanoparticle using microwave irradiation as photocatalayst for the degradation of Alizarin Red S. J Mol Struct 1113:174–181. https://doi.org/10.1016/j.molstruc.2016.01.053
7. DesMarias TL, Costa M (2019) Mechanisms of chromium-induced toxicity. Curr Opin Toxicol 14:1–7. https://doi.org/10.1016/j.cotox.2019.05.003
8. Dozzi MV, Saccomanni A, Selli E (2012) Cr(VI) photocatalytic reduction: Effects of simultaneous organics oxidation and of gold nanoparticles photodeposition on TiO_2. J Hazard Mater 211–212:188–195. https://doi.org/10.1016/j.jhazmat.2011.09.038
9. Dunkle SS, Helmich RJ, Suslick KS (2009) $BiVO_4$ as a visible-light photocatalyst prepared by ultrasonic spray pyrolysis. J Phys Chem C 113:11980–11983. https://doi.org/10.1021/jp903757x

10. Durán-Álvarez JC, Avella E, Ramírez-Zamora RM, Zanella R (2016) Photocatalytic degradation of ciprofloxacin using mono- (Au, Ag and Cu) and bi- (Au-Ag and Au-Cu) metallic nanoparticles supported on TiO_2 under UV-C and simulated sunlight. Catal Today 266:175–187. https://doi.org/10.1016/j.cattod.2015.07.033
11. Durán-Álvarez JC, Martínez-Avelar C, González-Cervantes E et al (2020) Degradation and mineralization of oxytetracycline in pure and tap water under visible light irradiation using bismuth oxyiodides and the effect of depositing Au nanoparticles. J Photochem Photobiol A Chem 388:112163. https://doi.org/10.1016/j.jphotochem.2019.112163
12. He X, Li P (2020) Surface water pollution in the middle Chinese loess plateau with special focus on hexavalent chromium (Cr^{6+}): Occurrence, sources and health risks. Expo Heal 12:385–401. https://doi.org/10.1007/s12403-020-00344-x
13. Hori M, Shozugawa K, Matsuo M (2015) Reduction process of Cr(VI) by Fe(II) and humic acid analyzed using high time resolution XAFS analysis. J Hazard Mater 285:140–147. https://doi.org/10.1016/j.jhazmat.2014.11.047
14. Islam JB, Furukawa M, Tateishi I et al (2019) Photocatalytic reduction of hexavalent chromium with nanosized TiO_2 in presence of formic acid. ChemEngineering 3:1–10. https://doi.org/10.3390/chemengineering3020033
15. Islam JB, Furukawa M, Tateishi I et al (2021) Formic acid motivated photocatalytic reduction of Cr(VI) to Cr(III) with $ZnFe_2O_4$ nanoparticles under UV irradiation. Environ Technol (United Kingdom) 42:2740–2748. https://doi.org/10.1080/09593330.2020.1713902
16. Jaihindh DP, Thirumalraj B, Chen SM et al (2019) Facile synthesis of hierarchically nanostructured bismuth vanadate: An efficient photocatalyst for degradation and detection of hexavalent chromium. J Hazard Mater 367:647–657. https://doi.org/10.1016/j.jhazmat.2019.01.017
17. Jayaraj SK, Paramasivam T (2019) Surface engineering of Au decorated V_2O_5 nanorods-Enhanced photodegradation of Rh-6G under visible light with high cyclability and stability. J Environ Chem Eng 7:103512. https://doi.org/10.1016/j.jece.2019.103512
18. Jian J, Xu Y, Yang X et al (2019) Embedding laser generated nanocrystals in $BiVO_4$ photoanode for efficient photoelectrochemical water splitting. Nat Commun 10:1–9. https://doi.org/10.1038/s41467-019-10543-z
19. Kalanur SS, Seo H (2022) Work function tuned, surface Cs intercalated $BiVO_4$ for enhanced photoelectrochemical water splitting reactions. J Energy Chem 68:612–623. https://doi.org/10.1016/j.jechem.2021.12.039
20. Kamble GS, Ling YC (2020) Solvothermal synthesis of facet-dependent $BiVO_4$ photocatalyst with enhanced visible-light-driven photocatalytic degradation of organic pollutant: assessment of toxicity by zebrafish embryo. Sci Rep 10:1–11. https://doi.org/10.1038/s41598-020-69706-4
21. Lace A, Ryan D, Bowkett M, Cleary J (2019) Chromium monitoring in water by colorimetry using optimised 1,5-diphenylcarbazide method. Int J Environ Res Public Health 16:1803.

https://doi.org/10.3390/ijerph16101803

22. Liang J, Huang X, Yan J et al (2021) A review of the formation of Cr(VI) via Cr(III) oxidation in soils and groundwater. Sci Total Environ 774:145762. https://doi.org/10.1016/j.scitotenv.2021.145762
23. Litter MI (2017) Last advances on TiO_2-photocatalytic removal of chromium, uranium and arsenic. Curr Opin Green Sustain Chem 6:150–158. https://doi.org/10.1016/j.cogsc.2017.04.002
24. Malathi A, Madhavan J, Ashokkumar M, Arunachalam P (2018) A review on $BiVO_4$ photocatalyst: Activity enhancement methods for solar photocatalytic applications. Appl Catal A Gen 555:47–74. https://doi.org/10.1016/j.apcata.2018.02.010
25. Matrosova EA, Bobrov AV, Bindi L (2020) basics of geochemistry and mineralogy of chromium. Geochemistry of Chromium in the Earth's Mantle. Springer Geology, pp 5–36
26. Meng X, Zhang Z (2016) Bismuth-based photocatalytic semiconductors: Introduction, challenges and possible approaches. J Mol Catal A Chem 423:533–549. https://doi.org/10.1016/j.molcata.2016.07.030
27. Nguyen TD, Hong SS (2020) Facile solvothermal synthesis of monoclinic-tetragonal heterostructured $BiVO_4$ for photodegradation of rhodamine B. Catal Commun 136:105920. https://doi.org/10.1016/j.catcom.2019.105920
28. Obregón S, Caballero A, Colón G (2012) Hydrothermal synthesis of $BiVO_4$: Structural and morphological influence on the photocatalytic activity. Appl Catal B Environ 117–118:59–66. https://doi.org/10.1016/j.apcatb.2011.12.037
29. Oros-Ruiz S, Zanella R, Collins SE et al (2014) Photocatalytic hydrogen production by Au-M_xO_y (MAg, Cu, Ni) catalysts supported on TiO_2. Catal Commun 47:1–6. https://doi.org/10.1016/j.catcom.2013.12.033
30. Owlad M, Aroua MK, Daud WAW, Baroutian S (2009) Removal of hexavalent chromium-contaminated water and wastewater: A review. Water Air Soil Pollut 200:59–77. https://doi.org/10.1007/s11270-008-9893-7
31. Perraki M, Vasileiou E, Bartzas G (2021) Tracing the origin of chromium in groundwater: Current and new perspectives. Curr Opin Environ Sci Heal 22:100267. https://doi.org/10.1016/j.coesh.2021.100267
32. Primo A, Corma A, García H (2011) Titania supported gold nanoparticles as photocatalyst. Phys Chem Chem Phys 13:886–910. https://doi.org/10.1039/c0cp00917b
33. Rengaraj S, Venkataraj S, Yeon JW et al (2007) Preparation, characterization and application of Nd-TiO_2 photocatalyst for the reduction of Cr(VI) under UV light illumination. Appl Catal B Environ 77:157–165. https://doi.org/10.1016/j.apcatb.2007.07.016
34. Saison T, Chemin N, Chanéac C et al (2015) New insights into $BiVO_4$ properties as visible light photocatalyst. J Phys Chem C 119:12967–12977. https://doi.org/10.1021/acs.jpcc.5b01468
35. Shen Y, Huang M, Huang Y et al (2010) The synthesis of bismuth vanadate powders and their photocatalytic properties under visible light irradiation. J Alloys Compd 496:287–292.

https://doi.org/10.1016/j.jallcom.2010.01.144

36. Sun S, Wang W, Li D et al (2014) Solar light driven pure water splitting on quantum sized $BiVO_4$ without any cocatalyst. ACS Catal 4:3498–3503. https://doi.org/10.1021/cs501076a
37. Teklay A (2016) Physiological effect of chromium exposure: A review. Int J Food Sci Nutr Diet S7:1–11
38. Tumolo M, Ancona V, De Paola D et al (2020) Chromium pollution in European water, sources, health risk, and remediation strategies: An overview. Int J Environ Res Public Health 17:1–25. https://doi.org/10.3390/ijerph17155438
39. Ugulu I, Khan ZI, Safdar H et al (2021) Chromium bioaccumulation by plants and grazing livestock as affected by the application of sewage irrigation water: Implications to the food chain and health risk. Int J Environ Res 15:261–274. https://doi.org/10.1007/s41742-021-00311-7
40. Van CN, Chang WS, Chen JW et al (2015) Heteroepitaxial approach to explore charge dynamics across Au/$BiVO_4$ interface for photoactivity enhancement. Nano Energy 15:625–633. https://doi.org/10.1016/j.nanoen.2015.05.024
41. Wang M, Shen S, Li L et al (2017) Effects of sacrificial reagents on photocatalytic hydrogen evolution over different photocatalysts. J Mater Sci 52:5155–5164. https://doi.org/10.1007/s10853-017-0752-z
42. Wang P, Zheng JY, Zhang D, Kang YS (2015) Selective construction of junctions on different facets of $BiVO_4$ for enhancing photo-activity. New J Chem 39:9918–9925. https://doi.org/10.1039/c5nj01836f
43. Wei Y, Zhang Y, Geng W et al (2019) Efficient bifunctional piezocatalysis of Au/$BiVO_4$ for simultaneous removal of 4-chlorophenol and Cr(VI) in water. Appl Catal B Environ 259:118084. https://doi.org/10.1016/j.apcatb.2019.118084
44. Xie B, Zhang H, Cai P et al (2006) Simultaneous photocatalytic reduction of Cr(VI) and oxidation of phenol over monoclinic $BiVO_4$ under visible light irradiation. Chemosphere 63:956–963. https://doi.org/10.1016/j.chemosphere.2005.08.064
45. Xu H, Wu C, Li H et al (2009) Synthesis, characterization and photocatalytic activities of rare earth-loaded $BiVO_4$ catalysts. Appl Surf Sci 256:597–602. https://doi.org/10.1016/j.apsusc.2009.05.102
46. Xu X, Sun Y, Fan Z et al (2018) Mechanisms for $^{\cdot}O_2^-$ and $^{\cdot}OH$ production on flowerlike $BiVO_4$ photocatalysis based on electron spin resonance. Front Chem 6:1–12. https://doi.org/10.3389/fchem.2018.00064
47. Yu X, Fan X, Li Z, Liu J (2017) Synthesis of plasmonic Ti^{3+} doped Au/Cl-TiO_2 mesocrystals with enhanced visible light photocatalytic activity. Dalt Trans 46:11898–11904. https://doi.org/10.1039/c7dt02824e
48. Zanella R, Avella E, Ramírez-Zamora RM et al (2017) Enhanced photocatalytic degradation of sulfamethoxazole by deposition of Au, Ag and Cu metallic nanoparticles on TiO_2. Environ Technol (United Kingdom) 3330:1–12. https://doi.org/10.1080/09593330.2017.1354926

49. Zanella R, Giorgio S, Henry CR, Louis C (2002) Alternative methods for the preparation of gold nanoparticles supported on TiO_2. J Phys Chem B 106:7634–7642. https://doi.org/10.1021/jp0144810
50. Zhang A, Zhang J (2010) Characterization and photocatalytic properties of Au/$BiVO_4$ composites. J Alloys Compd 491:631–635. https://doi.org/10.1016/j.jallcom.2009.11.027
51. Zhang L, Sun J, Niu W, Cao F (2020) The synergetic role of rice straw in enhancing the process of Cr(VI) photoreduction by oxalic acid. Environ Pollut 265:115013. https://doi.org/10.1016/j.envpol.2020.115013
52. Zhao W, Liu Y, Wei Z et al (2016) Fabrication of a novel p-n heterojunction photocatalyst n-$BiVO_4$@p-MoS_2 with core-shell structure and its excellent visible-light photocatalytic reduction and oxidation activities. Appl Catal B Environ 185:242–252. https://doi.org/10.1016/j.apcatb.2015.12.023

Supplementary Information

Supplementary Information is not available with this version.

Figures

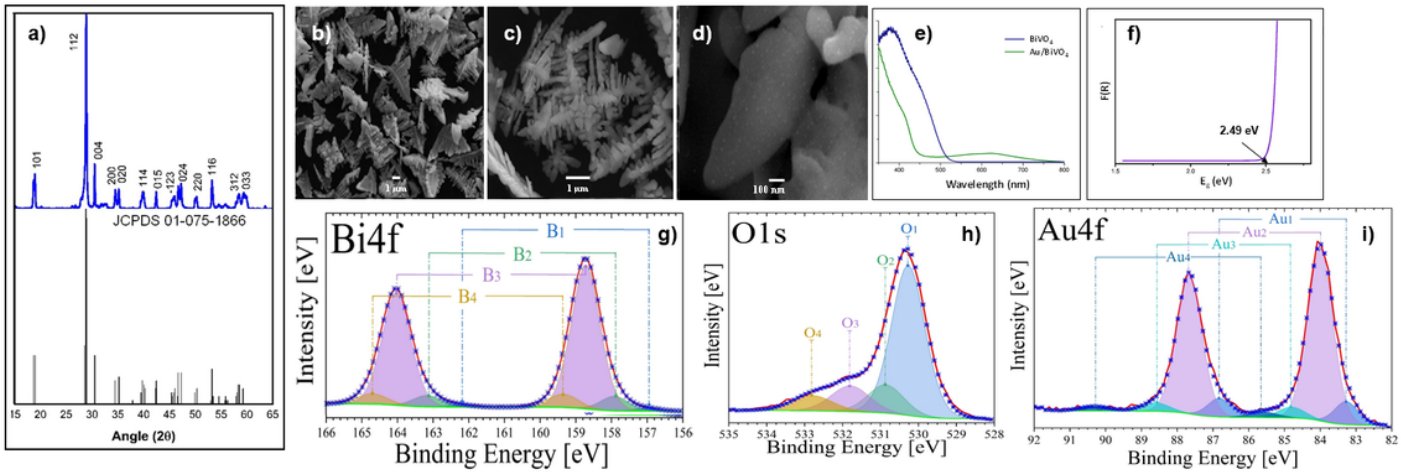

Figure 1

X-ray diffraction patterns of the synthesized $BiVO_4$ material (a), SEM images of the fern-leaf like $BiVO_4$ nanostructures (b-c), SEM micrography of the (1.0 wt. %) Au/$BiVO_4$ material (d), UV-visible light absorption spectra of the $BiVO_4$ and (1.0 wt. %) Au/$BiVO_4$ materials and Tauc plot used to determine the E_g value (e-f), and high-resolution XP spectra of the (1.0 wt. %) Au/$BiVO_4$ material, signals corresponding to Bi 4f (g), O 1s (h) and Au 4f (i)

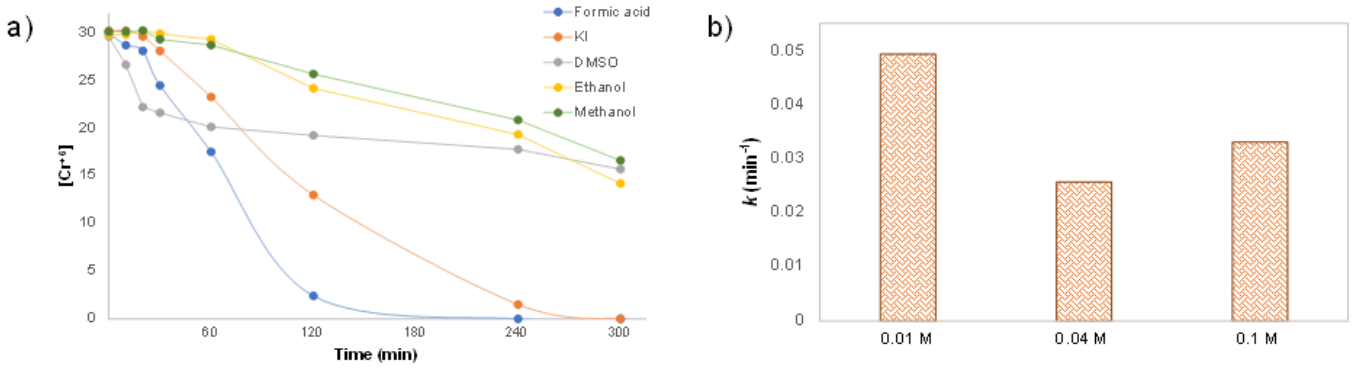

Figure 2

Photoreduction of Cr^{+6} in pure water using different sacrificial agents (a), and initial reaction rate constant (*k*) obtained by using different concentrations of formic acid as sacrificial agents (b)

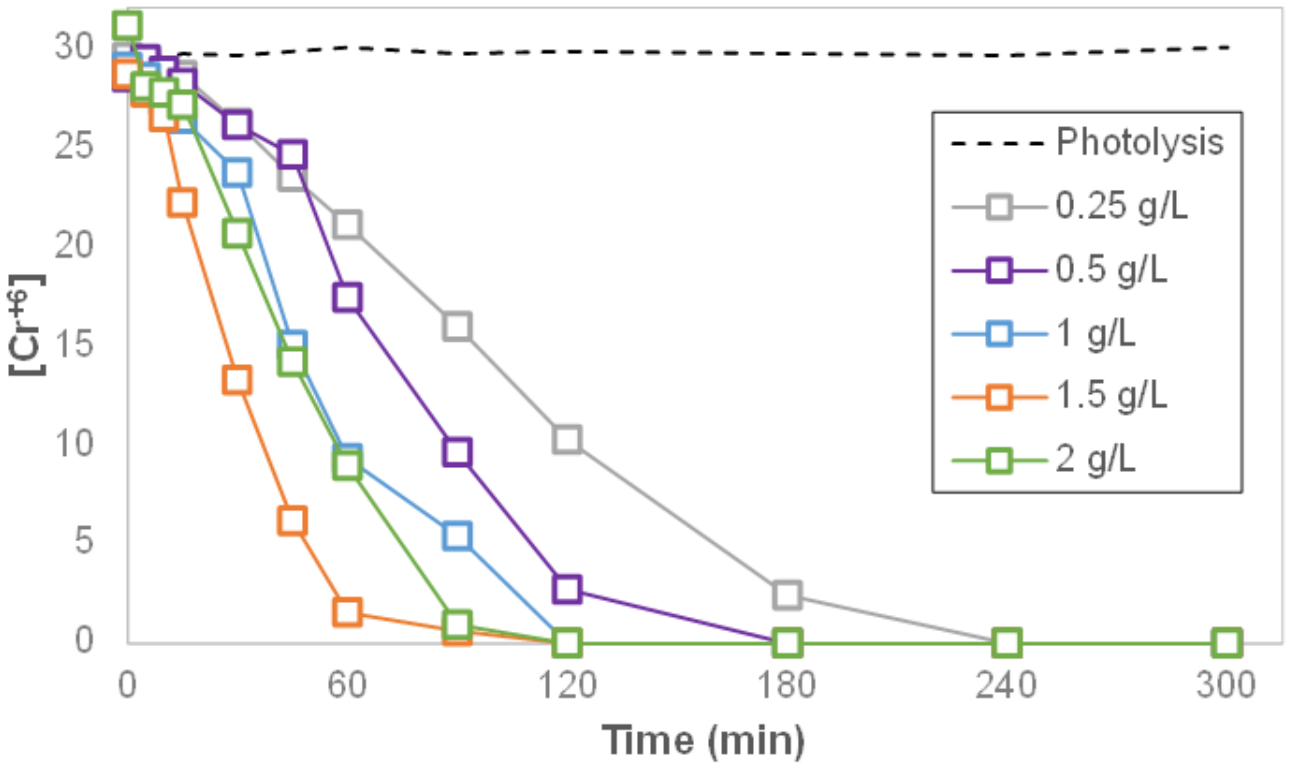

Figure 3

Photocatalytic reduction of Cr^{+6} using different $BiVO_4$ dosages

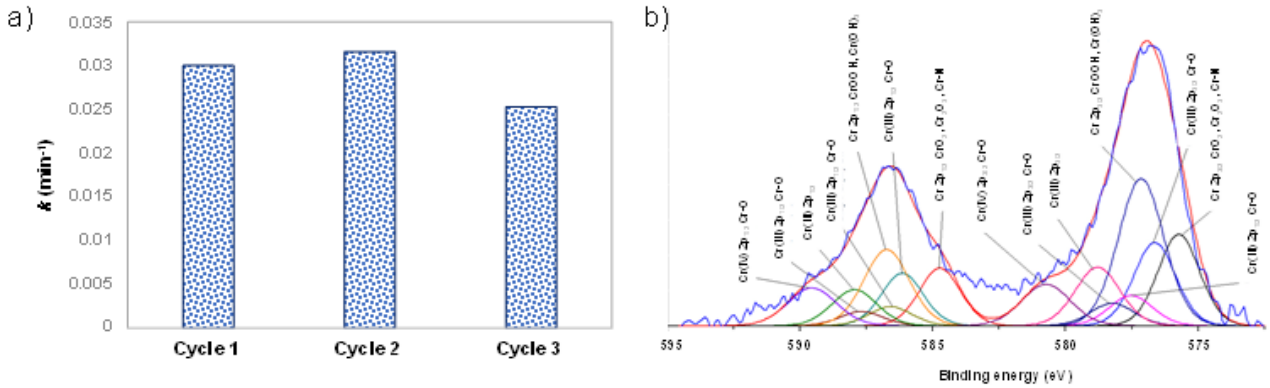

Figure 4

Initial conversion rate (k) across three consecutive photocatalysis reaction cycles (a), and high-resolution XP spectrum, at the Cr 2p window, of the $BiVO_4$ material after three consecutive reaction cycles (b)

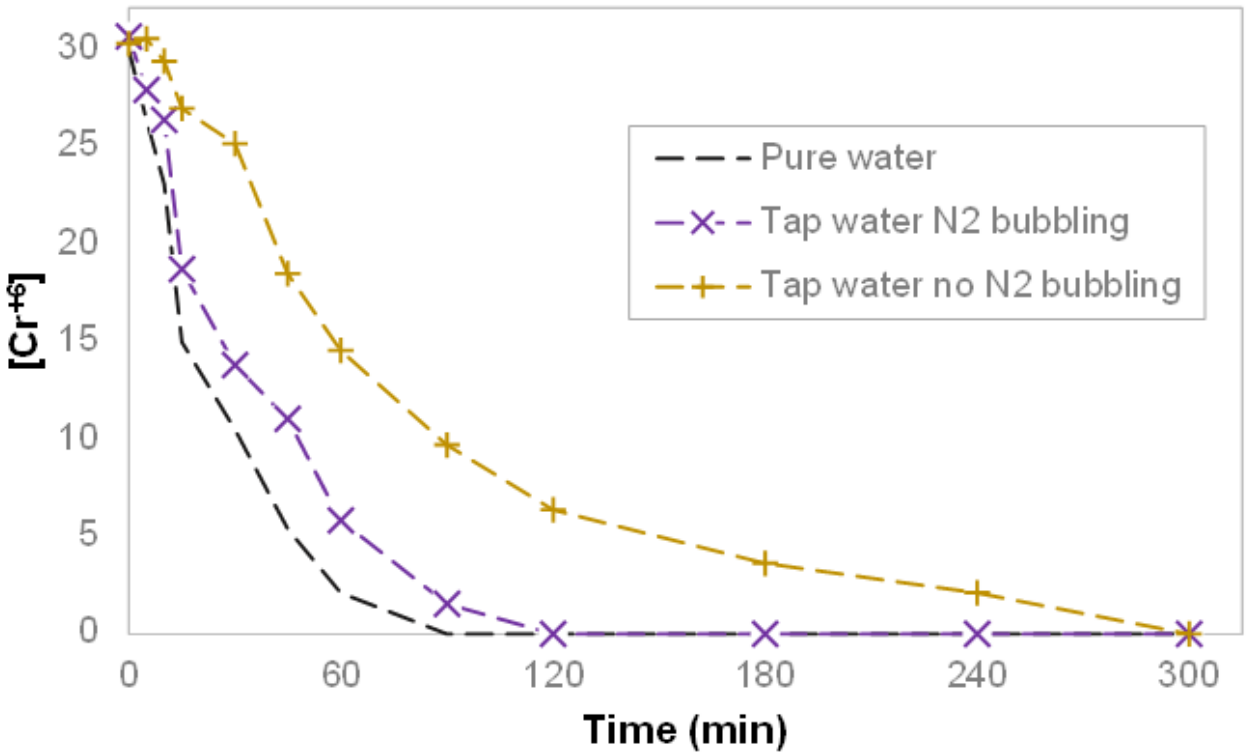

Figure 5

Photocatalytic reduction of Cr^{+6} in tap water using the optimal reaction conditions. Comparison of the reaction kinetics with pure water and in tap water with and without air purging by bubbling N_2